Interface-resolved simulations of the confinement effect on the sedimentation of a sphere in yield-stress fluids

Mohammad Sarabian[a,*], Marco E. Rosti[b], Luca Brandt[c,d]

[a] *Department of Biomedical Engineering, University of Arizona, Tucson, Az 85719, USA*
[b] *Complex Fluids and Flows Unit, Okinawa Institute of Science and Technology Graduate University, 1919-1 Tancha, Onna-son, Okinawa 904-0495, Japan*
[c] *FLOW and SeRC (Swedish e-Science Research Centre), Department of Engineering Mechanics KTH, SE 100 44 Stockholm, Sweden*
[d] *Department of Energy and Process Engineering, Norwegian University of Science and Technology (NTNU), Trondheim, Norway*

Abstract

We perform three-dimensional numerical simulations to investigate the confinement effect on the sedimentation of a single sphere in an otherwise quiescent yield stress fluid, in the presence of finite elasticity and weak inertia. The carrier fluid is modeled using the elastoviscoplastic constitutive laws proposed by Saramito [1]. The additional elastic stress tensor is fully coupled with the flow equation, while the rigid particle is represented by an immersed boundary method. The simulations show the faster relaxation of the fluid velocity and the progressive translation of the location of the negative wake downstream of the sphere as the bounding walls are brought closer to the particle. Moreover, the sphere drag decreases by increasing the particle-wall distance. We show that the confinement ratio (ratio of the gap between rigid confining walls and the sphere radius) reaches a critical value beyond which the wall-effect on the particle and flow dynamics becomes negligible. The key finding here is that the critical confinement ratio and the maximum variation of the Stokes drag with confinement ratio are weakly dependent on the level of material elasticity and plasticity for a certain range of material parameters. Finally, we propose an expression for the Stokes drag coefficient, as a function of material plasticity

*Corresponding author
Email address: msarabian@email.arizona.edu (Mohammad Sarabian)

and confinement ratio.

Keywords: particle, elastoviscoplastic material, fluid flows, confinement

1. Introduction

The understanding of suspensions of particles in materials which act either as liquids or as solids depending on the level of applied stress, i.e. the called "yield-stress" materials, has numerous applications in our everyday life [2], in engineering processes, *e.g.,* mineral slurries, food transport, drilling muds, microfluidics, fermentation processes; in biological systems, *e.g.,* biolocomotion, tissue engineering; and in natural phenomena, *e.g.,* natural muds and debris flows. In all of the mentioned applications, the particle transport and the particle sedimentation, due to any density mismatch between the object and the background yield-stress fluid, occur in the presence of confining walls and not in an infinite medium. Hence, the natural question that arises is how the flow dynamics and drag laws of a sphere settling in practical yield-stress fluids are affected by the presence of the confining walls.

It has been shown through several experimental measurements that elasticity plays an important role in the flow dynamics of the yielded region or of the liquid phase of yield-stress fluids such as foams, colloidal pastes, emulsions, Carbopol solutions, Laponite suspensions, and granular suspensions [3, 4, 5, 6, 7, 8, 9]. These soft materials, which exhibit elastic, viscous, and plastic effects simultaneously, have been characterized as elastoviscoplastic (EVP) [10, 11]. The elasticity of these types of soft materials manifests itself by breaking the fore-aft symmetry of the velocity field around a particle and with the appearance of a negative wake downstream of the settling spheres, as observed in experiments in Carbopol gels and Laponite suspensions under creeping conditions, see [4, 6]. This result was puzzling as the observed phenomena contradict the previous theoretical and computational results on creeping flows of spheres in pure viscoplastic fluids, *i.e.,* assuming no elastic effects [12, 13, 14]. Fraggedakis and co-workers [15] explained, for the first time, this contradiction by incorporating

elastic effects in a pure viscoplastic fluids using the EVP constitutive equations proposed by Saramito [1] by means of axisymmetric finite-element 2-D computations of a sphere settling in a large tube. These authors found that elasticity in the yield-stress fluid is enough to explain the experimental measurements, with no need to consider the thixotropy of the material. In addition, they demonstrated how the particle entrapment mechanism and the particle settling rate are influenced by the presence of elasticity, albeit in the absence of confining walls [15]. This behavior of EVP materials was later confirmed in the fully-resolved 3D numerical simulations of a sphere settling in an otherwise quiescent yield-stress fluid [16]. Simulations of the sedimentation of a single sphere in the absence and presence of a simple cross-shear flow in a yield-stress fluid at creeping flow condition [16] confirms that the elasticity is the leading mechanism for the previously observed fore-aft asymmetry in the velocity field around the sphere and the negative wake formation downstream of the sphere [4, 6]. Furthermore, it has been found that the fore-aft asymmetry in the velocity is less pronounced and the negative wake disappears when a linear cross-shear flow is imposed orthogonal to the settling direction [16]. Therefore, it is imperative to consider elastic effects inevitably present in laboratory yield-stress fluids to quantitatively capture the flow characteristics and the dynamics of a sphere settling in EVP materials in a numerical simulation.

In the case of particle sedimentation through a viscous Newtonian fluid with lateral confinement, it is known that the particle terminal velocity deviates from the theoretical predictions in an unbounded configuration, *i.e.,* Stokes law, following the well-known Faxen law [17]. Faxen [17] employed the method of images to obtain a series expansion and compute the drag on a sphere for different ratios of the gap between the walls and the diameter of the sphere. The analyses shows that the particle velocity dramatically decreases as the confining walls approach the particle [17]. Later, the steady-state settling velocities of single solid objects have been experimentally correlated to the gap/diameter ratio for various geometries, *i.e.,* triangular and square cylinders between parallel plates [18]. In a viscous Newtonian fluid, velocity perturbations from a settling sphere

extend to the Oseen length [19] (which scales with the ratio of particle radius and the particle Reynolds number) which may be larger than the gap between the bounding walls. When this is the case, the sphere drag is different than that of an infinite medium (unbounded fluid). Moreover, it has been observed through experimental measurements and fully-resolved particle simulations that the confining walls substantially affect the dynamics of the suspension flows in the Newtonian fluids through the structuring of the suspension into layers in the vicinity of the confining walls. [20, 21, 22, 23].

Wall-effects on the flow characteristics and the drag laws of a sphere settling in ideal yield-stress fluids, *i.e.,* in the absence of elastic effects, have been studied numerically and experimentally. In general, significant modifications of the shape and extent of the yield surface boundaries, as well as of the sphere drag, have been reported [24, 13, 25]. At fixed confinement ratio, defined as the ratio of the distance between two walls and the particle radius, the liquid zone surrounding the sphere shrinks with increasing plasticity, leaving thin viscous layers around the particle [24, 13]. For the case of a settling circular disk, it has been shown that these thin viscous layers resemble a cross-eyed owl [26]. Moreover, at fixed Bingham number, defined as the ratio of the yield stress to viscous stresses, the yielded zone that surrounds the particle extends to and interacts with the walls when decreasing the confinement ratio [24, 13].

The drag of a sphere settling in pure viscoplastic fluids is a function of the Bingham number and the confinement ratio: the drag grows by increasing the Bingham number at fixed confinement ratio [25, 13, 27, 28] and by decreasing the confinement ratio at fixed Bingham numbers [24, 13]. Nonetheless, for sufficiently large Bingham numbers, the drag coefficient becomes an independent function of the confinement ratio. This is observed when the small liquid layers are surrounded by a relatively large outer solid/plug region attached to the boundaries. In this configuration, at this high level of material plasticity, moving the confining walls closer to the sphere surface does not affect the drag forces and the flow dynamics significantly [13].

The particle and flow dynamics are influenced by the presence of the con-

fining walls in the case of viscoelastic fluids. In particular, the particle settles with smaller steady-state velocity in a confined medium filled than in an infinite medium [29, 30]. This is due to the development of elastic shear layers on the bounding walls when these are brought closer to the particle. Consequently, the elastic shear resistance is enhanced upon the inception of the particle motion which acts in the opposite direction of the sphere translation and hence resists the movement induced by the particle sedimentation. Typically, the wall effects and fluid elasticity are quantified by a drag correction factor which is a function of the confinement ratio and the elasticity [31]. Indeed, this factor measures the relative change in the sphere drag compared to the equivalent Stokes drag of the Newtonian fluid at vanishing particle Reynolds number. It has been found that the drag correction factor can be computed via a linear extrapolation of the drag correction factor for the case of the unbounded flow configuration at low levels of material elasticity [32]. For moderate elasticity levels, the confinement effects play a minor role in the particle dynamics and thus its drag can be well-approximated from the Newtonian counterpart at creeping flow conditions. However, at high levels of material elasticity, the magnitude of the drag enhancement is a strong function of both confinement ratio and the fluid elasticity [33]. The interested reader may consult [32] for further details.

To our knowledge, there is no prior computational or theoretical work in the literature on the complex interaction between bounding walls, flow and particle dynamics for a sphere settling in a practical yield-stress fluid that exhibits simultaneously elastic, plastic, and viscous behaviors. Therefore, the objective of the present work is to fill this gap by investigating the flow dynamics and the drag laws of a sphere settling in an EVP material in the presence of rigid confining walls. To this end, we solve the mobility problem numerically, *i.e.,* the particle is free to move due to the gravity, while the confining walls and the surrounding medium remain stationary.

The outline of our paper is as follows. In section 2, we define the problem and state the mechanical and mathematical modeling, justify the computational matrix, and introduce the boundary conditions and the numerical method. The

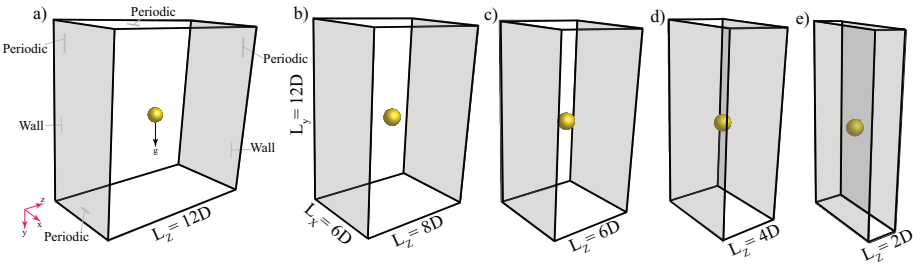

Figure 1: Schematic representation of a sphere settling in the EVP material inside rectangular boxes with different confinement ratios ζ: a) $\zeta = 24$, b) $\zeta = 16$, c) $\zeta = 12$, d) $\zeta = 8$, e) $\zeta = 4$. The boundary conditions are shown in panel a) and remain the same for all cases. The rigid bounding walls are indicated as transparent gray planes.

results are presented in section 3 and the main conclusions summarised in section 4.

2. Problem definition

We consider a single spherical particle with density ρ_p and radius R settling in an incompressible fluid that exhibits simultaneously elastic, viscous, and plastic behavior, *i.e.,* an elastoviscoplastic (EVP) fluid [10, 1, 11], at different confinement ratios ζ. This ratio is defined as the ratio of the distance between two bounding walls L_z, with z the wall-normal direction, and the particle radius R, *i.e.,* $\zeta = L_z/R$. The schematic representation of the problem along with the imposed boundary conditions are shown in figure 1. The computational domain is a rectangular box with length $12R$ in the spanwise x-direction and $24R$ in the streamwise (settling) y-direction, i.e. parallel to gravity, but with different lengths in the wall-normal z-direction (figure 1). To come to this choice, we have considered computational domains of size $L_x = 8R$, $12R$, and $16R$ in the spanwise x direction and $L_y = 20R$, $24R$, and $28R$ in the settling y direction and determined $L_x = 12R$ and $L_y = 24R$ as the minimum size of the computational domain where the particle does not interact with the wake of its periodic images while maintaining a reasonable computational efficiency. To study the wall effects on particle and fluid dynamics, we consider five confinement ratios,

i.e., $\zeta = 4, 8, 12, 16,$ and 24. For all the confinements, the computational domain size in the spanwise x and settling y directions remain unchanged, with imposed periodicity (see below). The particle is initially placed at the center of the box, translates from the resting position (zero initial velocity) and falls in an otherwise quiescent EVP material, and eventually reaches a constant (terminal) velocity U_p.

2.1. Mechanical model of the EVP material

The EVP material that we model here is a class of soft materials [10, 1, 11] that behaves similarly to a Hookean solid with elastic modulus G under small stresses [34], but flows like a viscoelastic fluid with relaxation time λ, above a critical stress, which is known as material yield-stress τ_y. We have resorted to the model proposed by Saramito [1] to simulate an EVP material which has been considered and validated in previous numerical simulations and shown to accurately follow the behavior of laboratory yield-stress fluids [11, 15, 16].

This model is composed of a friction element τ_y (material yield-stress), a spring element G (solid elastic modulus), two dashpots for the viscous stress of the solvent with viscosity η_s and of the EVP material with viscosity η_p. In brief, prior to yielding, the friction element remains rigid, and therefore the whole model predicts a Kelvin-Voigt viscoelastic solid with spring element G and dashpot with solvent viscosity η_s. Once the level of elastic strain energy exceeds the threshold value determined by the von Mises yielding criterion, the friction element breaks allowing deformation of all the other elements. After yielding, the material behaves like a viscoelastic fluid and the deformation is unbounded in time [1]. Hence, the EVP material is a combination of a viscoelastic solid (before yielding) and a viscoelastic fluid (after yielding). The interested reader may consult the work by Saramito [1] for a detailed physical interpretation of the mechanical model of EVP materials.

2.2. Mathematical formulation and boundary conditions

In this problem, the characteristic length scale is the particle radius R, the characteristic velocity scale is found by balancing viscous to buoyancy forces

$U_0 = \Delta\rho g R^2/\eta_0$, where $\Delta\rho$ is the density difference between the bead and the fluid, $\Delta\rho = \rho_p - \rho_f$ (ρ_f is the fluid density) and η_0 is the total material viscosity at zero shear-rate, computed as $\eta_0 = \eta_s + \eta_p$ (η_p is the polymer or plastic viscosity). The characteristic time scale is thus $t_0 = R/U_0 = \eta_0/\Delta\rho g R$. The stress and pressure fields are scaled with $\tau_0 = \Delta\rho g R$. The characteristic shear rate, which is the shear rate induced by the particle motion in the fluid is $\dot{\gamma}_0 = 1/t_0 = \Delta\rho g R/\eta_0$. The plastic viscosity η_p of the material is found from $\eta_p = \kappa\dot{\gamma}_0^{n-1}$, where $\kappa > 0$ is the consistency parameter, and $n > 0$ is the power law index [1] of the yield-stress fluid.

The dimensionless numbers of this problem are the particle Reynolds number $\mathrm{Re_p} = \frac{\rho_f \dot{\gamma}_0 R^2}{\eta_0}$, which is the ratio of the inertial to viscous forces, the Archimedes number $\mathrm{Ar} = \frac{\Delta\rho^2 g R^3}{\eta_0^2}$, that is the ratio of gravitational forces to viscous forces, the Bingham number $\mathrm{Bn} = \frac{\tau_y}{\Delta\rho g R}$, which is the ratio of the yield stress to the characteristic viscous stress τ_0, the Deborah number $\mathrm{De} = \frac{\lambda\Delta\rho g R}{\eta_0}$, which is the ratio of the material relaxation time λ to the characteristic time scale induced by the motion of the particle t_0 and is a measure of the material elasticity, the density ratio $\rho^o = \frac{\rho_p}{\rho_f}$, which is the ratio of particle to fluid density, the retardation parameter $\alpha = \frac{\eta_p}{\eta_0}$, which denotes the ratio of the solvent to the total viscosity, the confinement ratio $\zeta = L_z/R$, which is the ratio of wall-to-wall distance and the sphere radius, and the power law index of the yield-stress fluid n.

The flow dynamics is governed by the continuity and momentum equations, which read in the dimensionless form for an incompressible material

$$\nabla \cdot \boldsymbol{u} = 0, \tag{1}$$

$$\mathrm{Re_p}\left(\frac{\partial \boldsymbol{u}}{\partial t} + \boldsymbol{u}\cdot\nabla\boldsymbol{u}\right) = \nabla\cdot\left(-\left(p + \frac{1}{3}\,\mathrm{tr}\,(\boldsymbol{\tau}_{tot})\right)\boldsymbol{I} + \boldsymbol{\tau}_s + \boldsymbol{\tau}_{evp}\right) + \boldsymbol{f}, \tag{2}$$

where $\boldsymbol{u}$ is the fluid velocity vector, p is the generalized (nominal) pressure, $\boldsymbol{\tau}_{tot}$ is the total material stress, which consists of a solvent part $\boldsymbol{\tau}_s$ and an extra EVP part $\boldsymbol{\tau}_{evp}$ as $\boldsymbol{\tau}_{tot} = \boldsymbol{\tau}_s + \boldsymbol{\tau}_{evp}$, $\boldsymbol{I}$ is the identity tensor, and $\boldsymbol{f}$ is an

external body or immersed boundary (IB) force used to model the existence of the particle. The solvent stress tensor $\boldsymbol{\tau}_s = 2\,(1-\alpha)\,\boldsymbol{D}\,(\boldsymbol{u})$, where $\boldsymbol{D}\,(\boldsymbol{u})$ is the rate of deformation tensor defined as $\boldsymbol{D}\,(\boldsymbol{u}) = \frac{1}{2}\left(\nabla \boldsymbol{u} + \nabla \boldsymbol{u}^T\right)$. Note that, the extra stress tensor is not traceless in materials that exhibit elasticity, therefore the trace of the total stress should be considered in the momentum equation, *i.e.,* equation 2. Moreover, the nominal pressure p is identical to the pressure generated by the motion of the particle inside the box since by definition, the hydrostatic contribution cancels the gravity.

Saramito [1] proposed the following constitutive equation for the EVP extra stress tensor $\boldsymbol{\tau}_{evp}$

$$\mathrm{De}\,\overset{\nabla}{\boldsymbol{\tau}}_{evp} + \kappa_n\left(\boldsymbol{\tau}_{evp}\right)\boldsymbol{\tau}_{evp} - 2\alpha \boldsymbol{D}(\boldsymbol{u}) = 0, \tag{3}$$

where $\overset{\nabla}{\boldsymbol{\tau}}_{evp}$ is the upper convected derivative of the EVP stress field and is defined as:

$$\overset{\nabla}{\boldsymbol{\tau}}_{evp} = \frac{\partial \boldsymbol{\tau}_{evp}}{\partial t} + \mathbf{u}\cdot\nabla\boldsymbol{\tau}_{evp} - \left(\nabla \mathbf{u}\right)^T\cdot\boldsymbol{\tau}_{evp} - \boldsymbol{\tau}_{evp}\cdot\nabla\mathbf{u}. \tag{4}$$

In equation 3, $\kappa_n\left(\boldsymbol{\tau}_{evp}\right)$ is the plasticity criteria function, defined by the following relation [1]:

$$\kappa_n\left(\boldsymbol{\tau}_{evp}\right) = \max\left(0, \frac{|\tau_d| - \mathrm{Bn}}{(2\alpha)^{1-n}\,|\tau_d|^n}\right)^{\frac{1}{n}}, \tag{5}$$

where $|\tau_d|$ denotes the second invariant of the deviatoric part of the extra EVP stress tensor,

$$\boldsymbol{\tau}_d = \boldsymbol{\tau}_{evp} - \frac{1}{3}\,\mathrm{tr}(\boldsymbol{\tau}_{evp})\boldsymbol{I}. \tag{6}$$

As regards the settling particle, its translational and rotational velocities are computed by solving the Newton–Euler equations in the body-fixed reference frame:

$$\rho_p V_p \frac{d\boldsymbol{U}_p}{dt} = \oint_{\partial\Omega}\left(\boldsymbol{\tau}_{tot}\cdot\boldsymbol{n}\right)dA + \Delta\rho V_p \boldsymbol{g}, \tag{7}$$

$$\mathrm{I}_p\,\frac{d\boldsymbol{\omega}_p}{dt} = \oint_{\partial\Omega}\boldsymbol{r}\times\left(\boldsymbol{\tau}_{tot}\cdot\boldsymbol{n}\right)dA. \tag{8}$$

In equation 7, $\boldsymbol{U}_p$ is the particle velocity vector, V_p is the volume of the sphere, $\boldsymbol{n}$ is the unit normal vector at the particle surface $\partial\Omega$, and $\boldsymbol{g}$ is the gravitational acceleration vector. In equation 8, $\mathrm{I}_p = \frac{2}{5}\rho_p V_p R^2$ is the moment of inertia of the particle, $\boldsymbol{\omega}_p$ is the particle rotational velocity vector, and $\boldsymbol{r}$ represents the position vector relative to the particle centroid. The particle translational and angular velocity vectors $\boldsymbol{U}_p$ and $\boldsymbol{\omega}_p$ are computed in an inertial reference frame by adopting the rotation matrix formulation [35].

As shown in [15], in the context of EVP materials, it is imperative to consider the transient form of the governing equations, *i.e.,* the particle sedimenting from its inception until it reaches the steady-state. Consequently, all of our simulations are performed from zero initial conditions. In other words, the particle starts settling in an otherwise quiescent yield-stress fluid from zero translational and rotational velocities. A periodic boundary condition is applied for the velocity, pressure, and extra stress tensor in the spanwise x and settling y directions. In the wall-normal z-direction, we impose a no-slip boundary condition and homogeneous Neumann condition for pressure at the two bounding walls ($\partial p/\partial \boldsymbol{n} = 0$). A no flux condition is imposed normal to the confinement walls for the extra stress tensor. The no-slip/no-penetration boundary condition is satisfied at the sphere surface implicitly by using the multidirect forcing immersed boundary scheme [36]. Therefore, we simulate a rough particle, meaning that the slip is considered negligible on its rigid surface. The boundary conditions are reported in figure 1.

2.3. Computational matrix and its justification

We present a series of well-controlled high-fidelity numerical simulations for the problem of a single spherical particle settling through an EVP fluid at finite and small inertia. Our simulations are conducted at $\mathrm{Re_p} = 1$ and small Archimedes number, *i.e.,* $\mathrm{Ar} = 0.5$ to approximate the creeping flow conditions, while maintaining reasonable computational times. The density ratio ρ^o is held constant and equal to 1.5 since the density ratio, the particle Reynolds number, and the Archimedes number are related via $\rho^o = 1 + \frac{\mathrm{Ar}}{\mathrm{Re_p}}$. Note that the

maximum value of the particle Reynolds number based on the sphere terminal velocity, $\mathrm{Re}_{\mathrm{U_p}} = \frac{\rho_f U_p R}{\eta_0} = 0.2052$, which occurs at Bn $= 0$, De $= 1$, and $\zeta = 24$ (see figure 9 and equation 10, which show the relation between the Stokes drag coefficient $\mathrm{C_s}$ and the particle terminal velocity U_p). Therefore, the effect of inertia can be considered negligible. Moreover, we have previously shown that the simulation outputs at vanishing particle Reynolds number, *i.e.,* $\mathrm{Re_p} = 0$ and at small inertia, *i.e.,* $\mathrm{Re_p} = 1$ agree well with each other [16]. In this study, we model the EVP material as a yield-stress fluid with constant plastic viscosity η_p. Hence, the power-law index is equal to one, *i.e.,* $n = 1$, and the consistency parameter is a constant value and equal to seven, *i.e.,* $\kappa = 7$. Therefore, the retardation parameter is large $\alpha = 0.9$, which is in line with the value found for laboratory yield-stress fluids, where generally the solvent viscosity is negligible when compared to the plastic viscosity, *i.e.,* $\eta_p \gg \eta_s$ [15].

By performing axisymmetric transient computations in a cylindrical tube and imposing boundary condition on the tube centerline, it has been shown that the critical Bingham number, defined as the critical number above which the particle entrapment inside the yield-stress fluid occurs, or equivalently gravity number $\mathrm{Y_g} = 1.5\,\mathrm{Bn}$, is a function of the material elasticity, *i.e.,* De number. In creeping flow condition and $\zeta = 24$, the critical gravity number $\mathrm{Y_g^c}$ is related to De by the following equation [15]:

$$\frac{1}{\mathrm{Y_g^c}} = 1.2 + \frac{1.0}{0.176 + 0.135\,\mathrm{De}}. \tag{9}$$

In practical applications $0.5 \leq \mathrm{De} \leq 2$ [15]. Since our focus is mainly on the wall-effects on the particle and fluid dynamics, and not on the particle stoppage criterion, we study configurations below the critical condition, *i.e.,* $\mathrm{Y_g} < \mathrm{Y_g^c}$. Note that the critical gravity number $\mathrm{Y_g^c}$ presented in equation 9 is valid at $\zeta = 24$, and to our knowledge, there is no prior information in the literature on how this critical condition modifies at other confinement ratios for the EVP materials. Nonetheless, previous studies on purely viscoplastic fluids past a sphere contained in a cylindrical tube [25, 13, 24] or past a 2-D cylinder in a duct [37, 38] lead us to expect that the critical gravity number $\mathrm{Y_g^c}$ beyond which the

ζ	$\mathrm{Re_p}$	Ar	α	n	κ	De	Bn	$\mathrm{Bn^c}$ at De = 0.1	$\mathrm{Bn^c}$ at De = 0.5	$\mathrm{Bn^c}$ at De = 1.0
24	1.0	0.5	0.9	1.0	7.0	0.1, 0.5, 1.0	0.0, 0.0209, 0.0417	0.103	0.125	0.151
16	1.0	0.5	0.9	1.0	7.0	0.1, 0.5, 1.0	0.0, 0.0209, 0.0417	≤ 0.103	≤ 0.125	≤ 0.151
12	1.0	0.5	0.9	1.0	7.0	0.1, 0.5, 1.0	0.0, 0.0209, 0.0417	≤ 0.103	≤ 0.125	≤ 0.151
8	1.0	0.5	0.9	1.0	7.0	0.1, 0.5, 1.0	0.0, 0.0209, 0.0417	≤ 0.103	≤ 0.125	≤ 0.151
4	1.0	0.5	0.9	1.0	7.0	0.1, 0.5, 1.0	0.0, 0.0209, 0.0417	≤ 0.103	≤ 0.125	≤ 0.151

Table 1: Computational matrix adopted in the present study.

particle would not settle inside the EVP material is a decreasing function of the confinement ratio ζ at fixed elasticity. Note also that, at constant confinement ratio ζ and material plasticity, the critical gravity number $\mathrm{Y_g^c}$ is an increasing function of the material elasticity (see equation 9). In other words, at each ζ and Bn, the particle settles more easily and with faster rate at higher elasticity, *i.e.,* higher De number [15, 16].

The dimensionless parameters employed for the simulations presented here are reported in table 1. We present a series of fully-resolved simulations of a sphere settling in the EVP fluids at five different confinement ratios, $\zeta = 4, 8, 12, 16, 24$, at three Bingham numbers, $\mathrm{Bn} = 0.0, 0.0209, 0.0417$, and at three Deborah numbers, $\mathrm{De} = 0.1, 0.5, 1.0$. Therefore, we have performed a total of 45 simulations to investigate the wall effects on fluid and particle dynamics at different levels of material plasticity and elasticity. Performing the simulations at a small Deborah number ($\mathrm{De} = 0.1$) diminishes the problem complexity and hence enables us to interpret our predictions more easily as the elasticity effect can be neglected and the material assumed to behave like a pure viscoplastic fluid. The last three columns in table 1 report the critical Bingham number $\mathrm{Bn^c} = \frac{2}{3}\,\mathrm{Y_g^c}$ at each level of material elasticity (derived from equation 9): this is the value beyond which the particle would stop in a yield-stress fluid. It is noteworthy to mention that the critical condition presented in equation 9 is valid for the cylindrical tube configuration [15], and may be different for a rectangular box (our computational domain). Nonetheless, due to the lack of sufficient information in the literature, we presume that the same condition applies here and thus designed our computational matrix accordingly, with some safety margins. Indeed, our simulation results confirm that for all the cases

that are considered in this study, the sphere does not entrap inside the practical yield-stress fluid.

2.4. Numerical algorithm and code validation

The comprehensive details of the 3-D numerical algorithm, which is developed to handle transient, three-dimensional simulations of inertial EVP fluids with a large number of particles are explained in [39]. In brief, the governing equations of the EVP fluid, *i.e.,* equations 1-3 are integrated in time with a third-order Runge-Kutta (RK3) scheme for all terms except the pressure gradient for which the Crank–Nicolson scheme is used instead. RK3 is third-order accurate, low storage, and improves the numerical stability of the algorithm. These equations are solved on Cartesian, staggered, continuous, and uniform grids with the fractional-step method [40] in which all spatial derivatives are approximated with the second-order central-differencing scheme except for the advection terms in equation 3 where the fifth-order weighted essentially non-oscillatory (WENO) scheme is adopted [41]. Having the spatially continuous grid in the interior of the flow domain enables the use of a fast and highly scalable fast Poisson solver to enforce the condition of zero divergence for the velocity field. The coupling of the fluid and particle is performed with the immersed boundary method (IBM) proposed by Breugem [36]. The IBM allows solving the fluid governing equations on a Cartesian grid despite the presence of particles through adding an extra force $\boldsymbol{f}$ to the right-hand side of the momentum equations (see equation 2) and creating virtual boundaries inside the computational domain to mimic boundary conditions. This extra force is added in the vicinity of the solid particle to indirectly impose the no-slip/no-penetration (ns/np) boundary condition on the sphere surface [36]. The solid particle governing equations, *i.e.,* equations 7 and 8, are advanced in time with the same RK3 method with the relative position vector $\boldsymbol{r}$ independent of time.

We have adopted a grid resolution of 32 Eulerian grid points for particle diameter. Note that we have extensively tested the mesh convergence in our previous work (see [42]). The computational algorithm is coded in Fortran

Confinement ratio ζ	Number of cores	CPU hours
24	24	207360
16	16	138240
12	24	155520
8	16	34560
4	16	17280

Table 2: Summary of the computational resources required to complete the simulations. Compute system details: Processors: 2x AMD EPYC 7642 48-core (Rome), Processor Speed: 2.4GHz.

with the message-passing interface (MPI) extension for parallel execution on multi-processor machines. The number of cores and the central processing unit (CPU) hours required to achieve convergence and the steady-state solution at each confinement ratio ζ are reported in table 2.

The present three-dimensional numerical solver has been utilized and extensively validated in the past for particulate flows [43, 44, 45], non-Newtonian flows [42, 46, 47, 48, 16] and multiphase problems in non-Newtonian fluids [49]. The code has also been recently validated for suspensions of rigid and soft particles and droplets in EVP and viscoelastic fluids [39].

3. Results and discussion

In this section, we will first show how the confinement and its interaction with material elasticity and plasticity affect the flow features, together with the extent and shape of the yielded/unyielded zones around the settling sphere. Then, we will demonstrate the wall effect on the particle dynamics and how the particle terminal velocity changes in the presence of the confining walls at different levels of material plasticity and elasticity. Note that throughout this section, the particle diameter is denoted by $D = 2R$.

The criterion for the convergence of our simulations is chosen similar to the criterion presented in [50]: a particular simulation is converged if the L_∞ norm of the normal and shear stresses in the $y - z$ (settling) plane, *i.e.,* the τ_{yy} and

Bn ↓	De →	0.1	0.5	1	0.1	0.5	1
		$\hat{t}$	$\hat{t}$	$\hat{t}$	$\Delta\hat{y}$	$\Delta\hat{y}$	$\Delta\hat{y}$
0		48.3161	53.6872	56.3728	6.0610	6.9404	7.4688
0.0209		59.0583	75.1716	80.5427	4.2996	5.7210	6.4030
0.0417		80.4898	98.4390	112.7692	3.2202	3.3387	5.2406

Table 3: Dimensionless computational time $\hat{t}$ and the vertical displacement in the settling direction $\Delta\hat{y}$ required by the particle to reach the steady-state configuration at confinement $\zeta = 4$.

τ_{yz} components of the total stress tensor $\boldsymbol{\tau}_{tot}$, change less than 1%. The computational time required to satisfy this condition is different for each simulation case. Specifically, as the material elasticity is enhanced, or in other words, as the relaxation time of the macromolecular chains increases, the fullfilment of the convergence criterion is delayed and the simulations are longer than the lower elasticity simulation cases. Consequently, each simulation is terminated at a different time depending on the L_∞ norm of normal and shear stresses. Note also that the difference in the particle position at the steady-state shown in this section is due to the difference in the exact time that the corresponding simulation is deemed to have converged. The vertical distance travelled in the settling direction $\Delta\hat{y}$ during the dimensionless time $\hat{t} = t/t_0$ required by the sphere to reach the steady state for the different combinations of the dimensionless parameters (all 45 simulation cases) are reported in Table 3–7. In these tables, $\Delta\hat{y}$ is defined as: $\Delta\hat{y} = (y_s - y_0)/R$, where y_s is the position at which the terminal settling velocity is reached and y_0 the particle initial position. *i.e.,* center of the computational domain.

3.1. Flow features

First, we will show the variation of the fluid velocity field in the vicinity of the sphere by the confinement ratio ζ and material elasticity, *i.e.,* De number, when the plasticity, *i.e.,* the Bn number, is held constant and equal to Bn = 0.0417. In other words, the effect of confining rigid walls and material elasticity at

Bn ↓	De →	0.1	0.5	1	0.1	0.5	1
		$\hat{t}$	$\hat{t}$	$\hat{t}$	$\Delta\hat{y}$	$\Delta\hat{y}$	$\Delta\hat{y}$
0		37.5739	40.2595	42.9450	6.0934	6.7368	7.3714
0.0209		53.6872	91.2849	101.1486	4.7208	8.4496	9.8616
0.0417		59.0473	79.2609	91.2849	2.7920	4.1400	5.3594

Table 4: Dimensionless computational time $\hat{t}$ and the vertical displacement in the settling direction $\Delta\hat{y}$ required by the particle to reach the steady-state configuration at $\zeta = 8$.

Bn ↓	De →	0.1	0.5	1	0.1	0.5	1
		$\hat{t}$	$\hat{t}$	$\hat{t}$	$\Delta\hat{y}$	$\Delta\hat{y}$	$\Delta\hat{y}$
0		32.2028	48.3161	51.0017	5.5895	8.7177	9.4185
0.0209		64.4294	69.8005	71.1433	5.8081	6.6544	7.2294
0.0417		118.1403	121.3630	123.5114	5.6223	7.3951	7.5230

Table 5: Dimensionless computational time $\hat{t}$ and the vertical displacement in the settling direction $\Delta\hat{y}$ required by the particle to reach the steady-state configuration at $\zeta = 12$.

constant plasticity on the steady-state velocity field distribution around the sphere is shown in figure 2. The fluid velocity field around the sphere for various confinement ratios ζ at De $= 0.1$ and at De $= 1$ are displayed in the black and green box in figure 2. Note that due to the flow symmetry with respect to the $x - y$ plane, we have only shown the velocity distributions in the half central $y - z$ plane. In this figure, the velocity field is normalized by the characteristic velocity scale U_0 found by balancing viscous to buoyancy forces.

First we note that, for all confinement ratios and at a high degree of material elasticity, *i.e.,* De $= 1$, the well-known fore–aft asymmetry of the velocity field around the north and south poles of the sphere is lost with the formation of a negative wake, as previously observed in experiments [4, 6, 9, 28]. On the other hand, the loss of the fore-aft symmetry is less pronounced at low levels of elasticity, *i.e.,* De $= 0.1$ at all confinement ratios as the elasticity effect can be neglected and the EVP material can be well approximated by an ideal yield-stress fluid or pure viscoplastic fluid. The physical reason of such a behavior

Bn ↓	De →	0.1	0.5	1	0.1	0.5	1
		$\hat{t}$	$\hat{t}$	$\hat{t}$	$\Delta\hat{y}$	$\Delta\hat{y}$	$\Delta\hat{y}$
0		33.5456	37.5739	43.4821	6.4079	7.0147	8.3362
0.0209		59.0583	61.9422	64.4294	5.3386	5.9871	6.6624
0.0417		67.1149	91.4310	101.4338	3.2108	4.9339	6.3303

Table 6: Dimensionless computational time $\hat{t}$ and the vertical displacement in the settling direction $\Delta\hat{y}$ required by the particle to reach the steady-state configuration at $\zeta = 16$.

Bn ↓	De →	0.1	0.5	1	0.1	0.5	1
		$\hat{t}$	$\hat{t}$	$\hat{t}$	$\Delta\hat{y}$	$\Delta\hat{y}$	$\Delta\hat{y}$
0		28.2827	34.4681	45.3497	5.3195	6.1829	7.7296
0.0209		69.8005	70.8475	73.0232	6.3297	6.3993	7.6343
0.0417		54.2243	86.1729	89.6244	2.6095	4.6922	5.6876

Table 7: Dimensionless computational time $\hat{t}$ and the vertical displacement in the settling direction $\Delta\hat{y}$ required by the particle to reach the steady-state configuration at $\zeta = 24$.

has been revealed by Fraggedakis *et al.* [15], who showed that the material elasticity is the primary cause of fore-aft asymmetry of the velocity field and of the negative wake formation in laboratory yield-stress fluids and these are not related to the ageing of yield stress materials or thixotropy.

Changing the confinement ratio ζ affects the fluid velocity distribution around the particle once it settles in an EVP material at fixed De and Bn numbers. As depicted in figure 3 for the smallest and largest confinement ratios studied in this work, the velocity contour lines are visibly more packed when the walls are closer to the sphere. In particular, as the confining walls are brought closer to the sphere, the distribution of the velocity streamlines upstream and downstream of the sphere and in the equatorial plane on either side of the sphere is significantly affected. Note that for clarity, only the streamlines that surround the particle are shown in figure 3b) for the case of large confinement ratio, *i.e.,* $\zeta = 24$.

There are several important observations which can be made in reference to

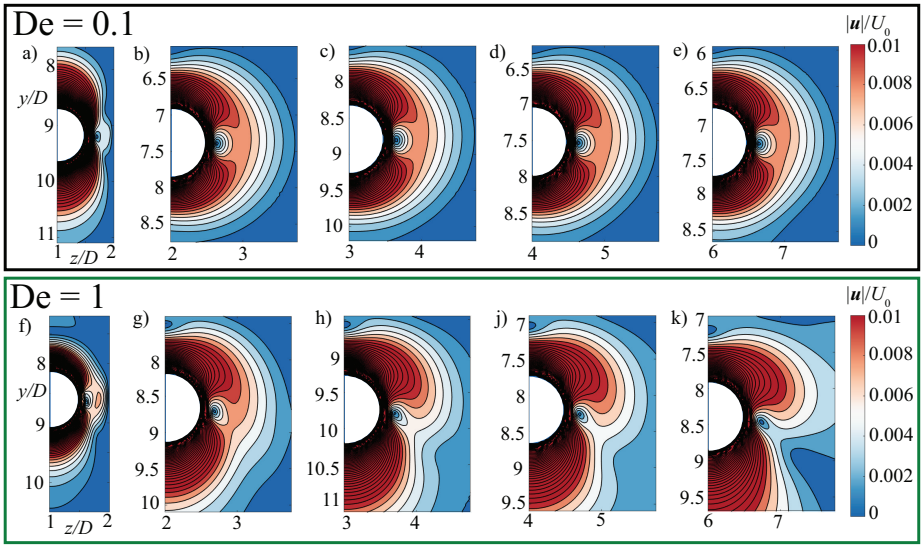

Figure 2: Normalized velocity magnitude around a sphere settling through an EVP fluid at Bn $= 0.0417$ in the y–z centreplane ($x = 6R$) and at various confinement ratios ζ and De numbers; a) $\zeta = 4$, De $= 0.1$, b) $\zeta = 8$, De $= 0.1$, c) $\zeta = 12$, De $= 0.1$, d) $\zeta = 16$, De $= 0.1$, e) $\zeta = 24$, De $= 0.1$, f) $\zeta = 4$, De $= 1$, g) $\zeta = 8$, De $= 1$, h) $\zeta = 12$, De $= 1$, j) $\zeta = 16$, De $= 1$, and k) $\zeta = 24$, De $= 1$.

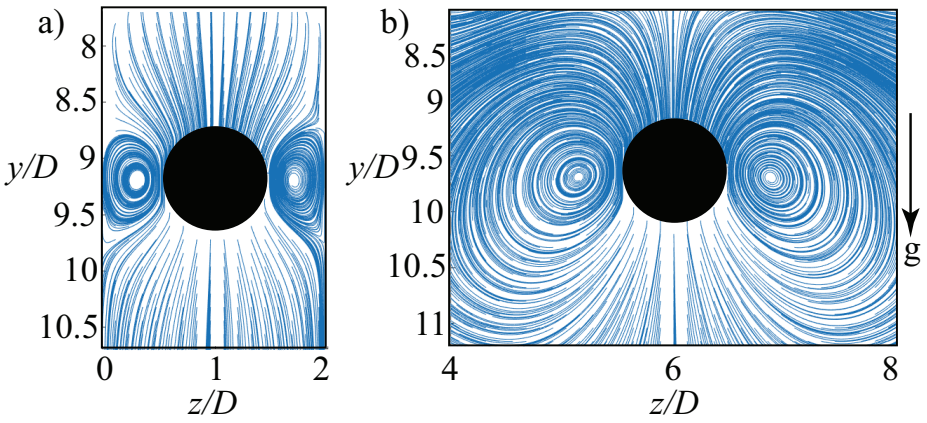

Figure 3: Velocity streamlines in the y–z centreplane ($x = 6R$) for the flow around a sphere settling through an EVP fluid at Bn $= 0.0417$ and De $= 1$ and at a) $\zeta = 4$, b) $\zeta = 24$. The velocity streamlines are the projection of the 3D streamlines on the central y–z plane.

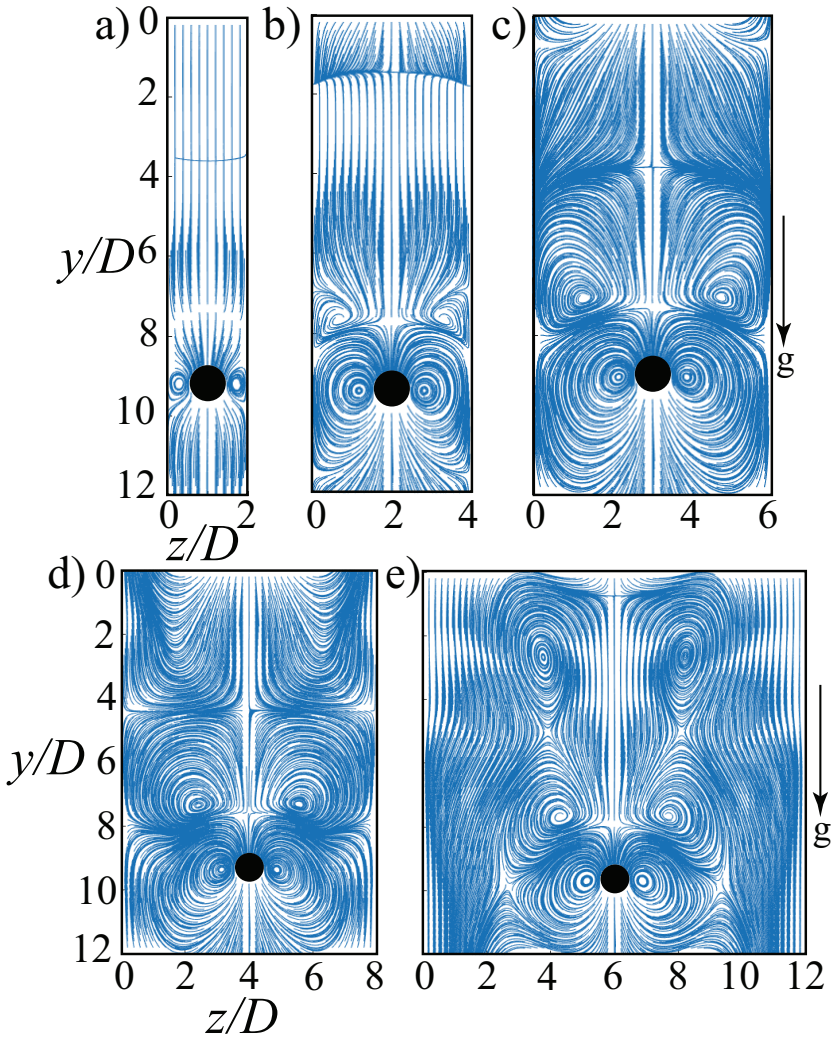

Figure 4: Velocity streamlines in the y–z centreplane ($x = 6R$) for a sphere settling through an EVP fluid at Bn = 0.0417 and De = 1 and at a) $\zeta = 4$, b) $\zeta = 8$, c) $\zeta = 12$, d) $\zeta = 16$, e) $\zeta = 24$.

figure 3. First, we observe that the recirculation zones can be seen in the equatorial plane and on either side of the sphere for both confinements. This flow behavior, which is a consequence of assuming a rough particle, *i.e.,* a particle with no-slip boundary condition, is in line with previous experimental mea-

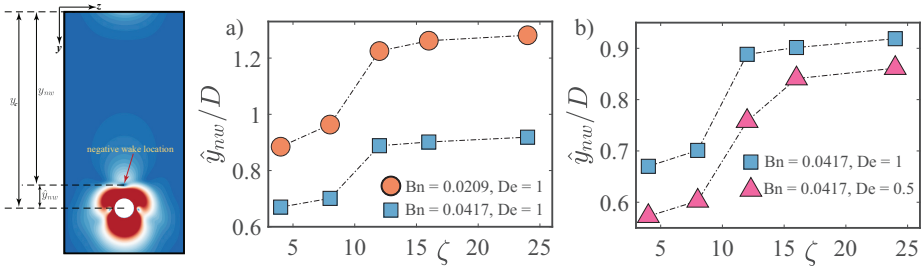

Figure 5: The evolution of the relative position of the negative wake, $\hat{y}_{nw}$, downstream of the particle in the streamwise direction y versus the confinement ratio ζ at a) constant De = 1 and two different Bn numbers, and b) constant Bn = 0.0417 and two different De numbers.

surements [9] and computations adopting either an extensive mesh refinement near the particle surface [15] or Cartesian grids with the immersed boundary approach [16]. Second, at a smaller confinement ratio, the recirculation zones interact with and extend to the channel walls, which leads the flow streamlines upstream and downstream of the sphere to be more packed and closer to the sphere surface. On the other hand, as the walls are brought further away from the particle, the recirculation zones do not extend to the channel walls and the flow streamlines remain unaffected by the motion of the particle close to the channel walls. This effect is also seen in figure 4 where we display results for all the confinement ratios studied here. Here, the material elasticity, and plasticity are held fixed as in figure 3, so that the variations of flow streamlines can be entirely attributed to the rigid wall effects. We also observe that new recirculation zones are created once the particle sediments in a less confined configuration as depicted in figure 4, where we show the existence of two and six recirculation regions for $\zeta = 4$ and $\zeta = 24$, respectively.

The effect of changing the confinement ratio ζ on the position of the negative wake downstream of the sphere at constant elasticity (De = 1) and two levels of plasticity and at fixed plasticity (Bn = 0.0417) and two degrees of material elasticity is illustrated in figure 5a and 5b. In this figure, the negative wake position is measured relative to the particle center at steady-state, *i.e.,* $\hat{y}_{nw} = y_c - y_{nw}$, where y_c is the particle center location and y_{nw} is the negative wake

location (see sketch in figure 5). By definition, the negative wake position is where the fluid velocity is opposite the particle velocity, downstream of the north pole of the sphere [15]. In other words, the negative wake position is defined as the specific point in the fluid medium where the velocity is approximately zero, before the direction of the fluid velocity is reversed and becomes opposite to the particle velocity. This position is also called "flow stagnation point" (see figure 6b).

The interaction between shear and normal stresses downstream of the sphere is shown to be the primary cause for the negative wake formation, with the normal stress relaxing faster than the shear stress away from the particle surface [see 15, 16, for more details in the case of limited confinement]. According to figure 5a and 5b, at lower confinement ratios ζ, when the confining walls are brought closer to the particle, the negative wake moves closer to the sphere north pole. This means that the relaxation of the shear stress downstream of the particle is delayed at lower confinements ζ (see also figure 10). This explains why the sphere drag increases or the particle settling rate decreases when bringing the channel walls closer to the sphere surface, as further discussed below in section 3.2 when considering the effect of the boundaries on the particle dynamics. According to figure 5a and 5b, translating the negative wake formation towards the north pole of the sphere by decreasing the confinement ratio ζ occurs at all combinations of material plasticity and elasticity studied here. Moreover, the relative position of the negative wake moves closer to the sphere north pole at elevated Bn number and at fixed confinement ratio ζ and De number (figure 5a). This is due to the fact that the unyielded region expands and approaches the surface of the sphere at higher Bn numbers (see figure 7). On the other hand, the negative wake moves further away from the sphere's north pole at higher levels of material elasticity and fixed plasticity and confinement ratio as shown in figure 5b. This behavior can be understood since the elasticity makes the sphere translate faster in the EVP materials [15, 16], and this is the result of increasing the volume of the yielded region in the medium at higher elasticity.

Next, we study how the formation of the negative wake downstream of the

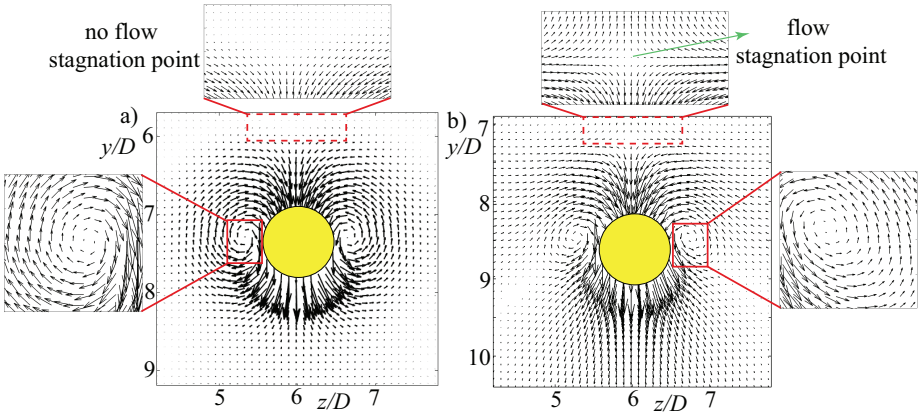

Figure 6: Velocity vectors around the sphere settling in an EVP material in the central $y-z$ plane at Bn $= 0.0417$ and $\zeta = 24$ at a) De $= 0.1$ and b) De $= 1$. The dashed and solid red boxes magnify the flow stagnation points and recirculation zones, respectively.

sphere is affected by changing the material elasticity, *i.e.,* De number, when the confinement ratio ζ and Bn number are held constant, see figure 6. As previously shown by Fraggedakis *et al.* [15] and later by Sarabian *et al.* [16], the existence of finite elasticity in the practical yield-stress fluids favors the negative wake formation downstream of the sphere, associated with the flow stagnation point. Therefore, at small De numbers, when elasticity becomes negligible and the EVP material behaves like a pure viscoplastic fluid, the negative wake disappears. The absence and presence of a negative wake at De $= 0.1$ and De $= 1$ are illustrated in figure 6a) and 6b). Since the Bn number and confinement ratio ζ are kept constant, then the negative wake formation at higher elasticity, *i.e.,* De $= 1$, in figure 6b) is solely due to the elasticity effect. The disappearance of the negative wake is associated to the recovering of the fore-aft symmetry of the velocity field around the sphere at lower elasticity as shown in figure 1a) and b).

Let us now focus on the evolution of the yield surface that surrounds the settling particle when changing the confinement ratio ζ and the Bn number when the De number is held constant. The extent and shape of the yielded/unyielded zones around the settling sphere are depicted in figure 7 where the red and blue

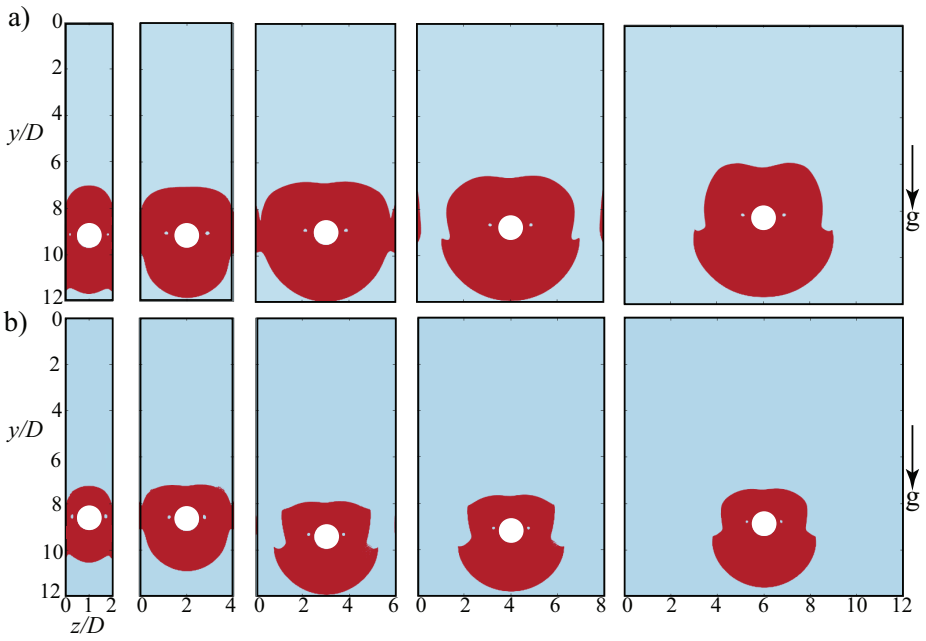

Figure 7: Evolution of the yield surface for flow of an EVP material around a rough particle for various confinement ratios ζ and Bn numbers and at constant elasticity De = 1 in the central $y-z$ plane. Red and blue color represent the yielded and unyielded regions. a) Bn = 0.0209, and b) Bn = 0.0417. In both panels a) and b) the figures from left to right indicate the yielded boundaries at $\zeta = 4$, $\zeta = 8$, $\zeta = 12$, $\zeta = 16$, and $\zeta = 24$.

colours in the figure indicate the regions of the EVP material that behaves as a liquid and solid, respectively. Note that since we perform 3-D numerical simulations, the yielded boundaries are 3-D surfaces, and figure 7 shows the projection of the unyielded surfaces onto the $y-z$ central plane at different confinements and Bn numbers. Furthermore, as mentioned previously, the difference in the sphere positions at different confinements and material plasticity is due to the difference in the time when the flow reaches the final steady state.

We observe the existence of two unyielded zones regardless of the confinement ratio and the degree of material plasticity. The first one is the unyielded envelope that surrounds the fluid zone and the second one is the solid island or solid ring in 3-D located in the liquid zone at the equator and on either side of the sphere.

Contrary to the case of 2-D cylinders, these unyielded rings are not rotating solid islands since these are the zones in which the second invariant of the deformation rate tensor is zero. Similarly to pure viscoplastic fluids [51, 12, 24, 13, 26], the outer unyielded envelope grows progressively with increasing plastic effects at fixed confinement ratio ζ and material elasticity. However, the particle arrest or stoppage mechanism in the EVP fluid is different from the pure viscoplastic fluids. Indeed, in the EVP material, the yield surface approaches the surface of the particle from the equator plane causing the particle to stop settling [15, 16]. Conversely, in the purely Bingham or Herschel–Bulkley fluids, the fluidization surface approaches the surface of the particle from its north and south poles [15].

For $\zeta = 4$ and 8, the resulting outer yield envelope extends to the channel walls for both Bn numbers under consideration, and hence the particle dynamics is significantly affected by the presence of the confining walls. A similar behavior has been previously reported for the case of a particle settling in a tube filled with the Bingham plastic [13] and Herschel–Bulkley fluids [24]. The yield surface, however, does not intersect the channel walls for $\zeta \geq 16$ and $\zeta \geq 12$ at Bn $= 0.0209$ and Bn $= 0.0417$ respectively. For the case $\zeta = 16$, an interesting phenomenon occurs near the channel walls for the smallest Bn $= 0.0209$: the material is sheared next to the wall (yielded) and then again around the particle and solid islands, having a plug zone in between, where the shear rate is zero. For both Bn numbers, the outer yield surface does not intersect the channel walls for the confinement ratio $\zeta = 24$ even at the smallest Bn number studied here. Consequently, the effect of the confinement on the particle dynamics is negligible at this ratio. This is in agreement with previous axisymmetric particle-settling computations in an EVP material [15]. Moreover, our simulations show that the yield surface shrinks by decreasing material elasticity at constant plasticity and confinement ratio. This behavior is however not discussed here as it was already discussed in detail in [15, 16]. Specifically, at higher De numbers, the increased elastic stresses in the medium enable the material to more easily exceed the von-Mises yielding criterion. Therefore, elasticity helps the sphere to

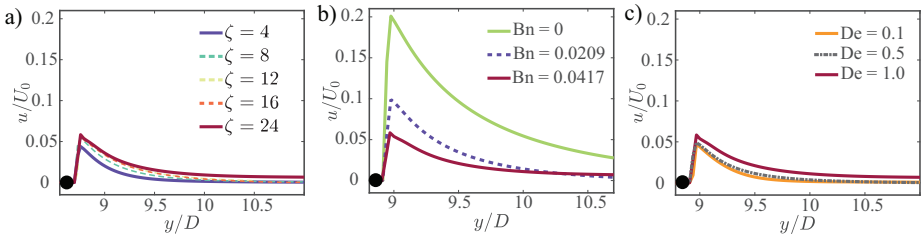

Figure 8: Distribution of the normalized fluid velocity magnitude upstream of the particle (sphere's south pole) as a function of the distance in the settling direction y at a) various confinement ratio ζ and constant Bn $= 0.0417$, De $= 1.0$. b) Effect of various Bn number at constant $\zeta = 24$ and De $= 1.0$. c) Effect of various De numbers at constant $\zeta = 24$ and Bn $= 0.0417$. In all the panels, the sphere is only shown for major clarity and is not scaled accordingly.

translate faster in the EVP material. This is further discussed in section 3.2.

The fluid velocity distribution upstream of the particle, *i.e.,* the south pole of the sphere, and how it relaxes far away from the sphere south pole at various confinement ratios ζ, Bn, and De numbers are illustrated in figure 8. In the different panels, we investigate how the fluid velocity distribution upstream of the sphere is altered when the particle settles at various confinement ratios ζ and fixed De and Bn numbers, when it sediments in the EVP fluid with different Bn number at fixed ζ and De number and when it settles in the material with different De number while ζ and Bn number are kept constant.

Panel a) of the figure reveals that the fluid velocity on the particle surface and on the south pole of the sphere decreases at fixed material plasticity and elasticity as the confining channel walls are brought closer to the sphere. This was expected from the visualisations above since at lower confinement ratios the yield surface interacts with the channel walls and both the flow and particle dynamics are greatly affected by the presence of the walls. Moreover, the flow streamlines (shown in figures 3 and 4), as well as the location of the negative wake in the medium (shown in figure 5), are modified by the presence of the walls and hence the sphere settles with a lower rate at lower confinement ratios. This implies that the velocity of the fluid element attached to the south pole of the

sphere decreases at lower confinement ratio ζ as shown in figure 8a). In addition, we observe that the fluid velocity relaxes faster at smaller confinements and therefore the change in the fluid velocity magnitude and of the direction of the streamlines is more abrupt as the sphere settles in a more confined configuration.

As shown in figure 8b), the fluid behavior when varying the material plastic effects at fixed confinement ratio ζ and material elasticity is qualitatively similar to that observed when varying the confinement ratio and fixing the material plasticity and elasticity. Specifically, the fluid velocity on the south pole of the sphere decreases with the plasticity, *i.e.,* with the Bn number. This behavior is due to the fact that at a higher degree of material plasticity, the volume of the yielded zone in the medium shrinks, and the yield boundary approaches the sphere surface causing the sphere to settle at a smaller rate. Thus, the particle settles slower when either fixing the material plasticity and bringing the channel walls closer to the sphere or fixing the confinement ratio and increasing the material plasticity. Nonetheless, contrary to what has been conjectured before [15], the flow and particle behavior are not in quantitative agreement with each other since the change in fluid velocity is more significant for variations of the material plasticity at constant confinement ratio than for a change of the confinement ratio at constant material plasticity, as can be seen comparing figures 8a) and b). Moreover, similarly to the results in figure 8a), the fluid velocity relaxes faster at higher Bn numbers and fixed confinement ratio ζ since now the outer yield envelope is closer to particle and the solid zone in the medium has larger size at a higher Bn number, *i.e.*, the regions of zero shear rate are larger at higher Bn numbers.

The fluid velocity is an increasing function of material elasticity at constant confinement ratio and material plasticity as shown in figure 8c). The physical reason for such a behavior is that as the elasticity of the material is increased, the volume of the liquid phase around the sphere increases too, as the increased elastic stresses in the medium lead to satisfying the yielding criterion more easily. Hence, the outer yielded envelope gets far away from the sphere surface at higher elasticity and this contributes to the increase in velocity magnitude

as the elastic effects increase in the medium [15, 16]. In other words, elasticity aids the sphere to translate faster in an EVP material. One of the consequences of having a larger yielded zone in the medium around the particle is that the distance in the settling direction y between the sphere surface and the location in the medium where the streamlines remain unaffected in the presence of the particle increases. This is evident in figure 8. For instance, in figure 8b) and 8c) the fluid velocity relaxes at larger distance y from the sphere surface at the smallest Bn number and constant confinement ratio ζ and De number (solid red line in figure 8b) or at largest De number and constant confinement ratio ζ and Bn number (solid red line in figure 8c), the volume of the yielded zone being the largest in both conditions, *i.e.,* at Bn $= 0$, $\zeta = 24$, De $= 1.0$ (figure 8b) and De $= 1.0$, $\zeta = 24$, Bn $= 0.0417$ (figure 8c).

3.2. Particle dynamics

For a single sphere settling in an EVP material at constant Archimedes number Ar $= 0.5$, the settling rate at steady-state condition or its terminal velocity, and the Stokes drag coefficient C_s are a function of confinement ratio, the material plasticity, and elasticity, *i.e.,* $U_p = U_p\,(\zeta, \mathrm{Bn}, \mathrm{De})$, and $C_s = C_s\,(\zeta, \mathrm{Bn}, \mathrm{De})$. Note also that, at steady-state, the sphere angular velocity $\boldsymbol{\omega_p}$ is zero for all the cases. The variation of the Stokes drag coefficient C_s resulting from the present study along with the comparison with the numerical data from the previous study [15] is illustrated in figure 9 versus the confinement ratio ζ, for the values of Bn and De under consideration, which probably represents the main results of this work. Moreover, the variation of the Stokes drag coefficient C_s with the confinement ratio ζ and the material plasticity, *i.e.,* Bn number, obtained with the correlation in equation 13 is shown as black dotted lines in figure 9.

The Stokes drag coefficient C_s classically provides information about the motion of rigid particles in non-Newtonian fluids. This measures the deviation of the drag force experienced in an otherwise quiescent EVP fluid from the Stokes drag force, *i.e.,* the drag force exerted on a sphere moving through a viscous Newtonian fluid at creeping flow condition and in an infinite medium

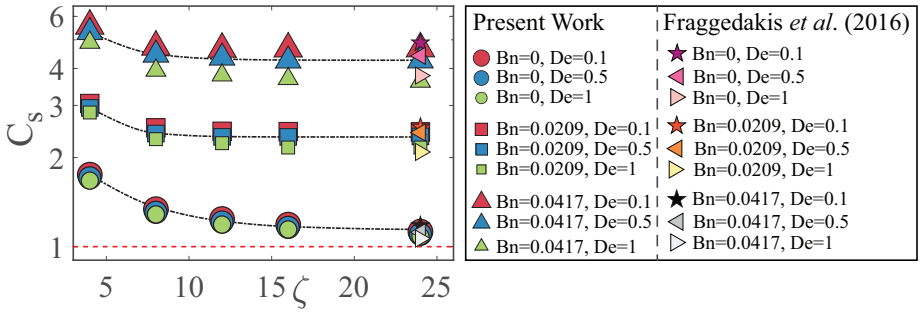

Figure 9: Stokes drag coefficient C_s versus confinement ratio ζ for the various Bn and De numbers under investigation, see legend. The value $C_s = 1$ is indicated by a red dashed horizontal line. The black dotted lines represent the variation of C_s with confinement ratio ζ and Bn number from correlation (13). The Stokes drag coefficient C_s at $\zeta = 24$ and various Bn and De numbers resulting from the present work is compared against the same quantity and the same Bn and De numbers from Fraggedakis *et al.* [15].

(no confining walls) and it is defined as [12]:

$$C_s = \frac{F_d}{6\pi\eta_0 U_p R} = \frac{2}{9}\frac{U_0}{U_p}. \tag{10}$$

The total drag force exerted on the particle by the surrounding fluid, F_d, is computed by balancing the weight of the sphere at steady state (zero acceleration), *i.e.*, $F_d = \frac{4}{3}\pi R^3 g\Delta\rho$. It follows from this definition that $C_s = 1$ corresponds to the Newtonian fluid case.

According to figure 9, at constant Bn and De numbers, the Stokes drag coefficient increases, or equivalently the particle terminal velocity U_p is reduced when reducing the confinement ratio ζ. Therefore, the particle dynamics are significantly affected by the presence of the channel walls. Our simulations show that, in general, the behavior of the Stokes drag coefficient C_s and of particle terminal velocity U_p with the confinement ratio ζ is similar for each Bn and De number studied here. The change in particle dynamics is more pronounced at $\zeta = 4$ as compared to other confinements, regardless of the degrees of material plasticity and elasticity. A similar trend has been observed previously for the particle settling through Bingham plastic fluids in a tube: in this case, the Stokes drag coefficient at constant Bn number is substantially higher for the

diameter ratio (ratio of the tube and sphere radius) of 2 than for larger ratios [13].

In the case of a Newtonian fluid, the well-known Faxen law [17] shows that the particle settling rate decreases once the confinement walls approach the particle radius. The same scenario is observed when the channel is filled with viscoelastic fluids, with the particle terminal velocity always smaller than that observed when it settles in an infinite medium [29, 30]. Here, we observe that the same behavior arises also when the sphere settles in EVP fluids.

The Stokes drag coefficient is an increasing function of the material plasticity at fixed elasticity and confinement ratio as shown in figure 9. At fixed confinement and material elasticity and elevated level of plasticity, the surface of the particle is approached by the yielded surface (shown in figure 7). Consequently, since the outer yield envelop behaves like an elastic wall in the context of an EVP fluid, increasing the Bn number is similar to enforcing the sphere to settle in a more confined channel with elastic walls. Hence, the Stokes drag increases. On the other hand, the Stokes drag coefficient is a decreasing function of material elasticity at fixed plasticity and confinement ratio as depicted in figure 9. Our observation is in agreement with previous transient 2-D axisymmetric finite-element computations [15] or 3-D fully-resolved computations [16] performed at large confinement ratio $\zeta = 24$. Our simulations demonstrate that the decrease of the Stokes drag coefficient with the material elasticity at constant Bn number and confinement ratio ζ is observed regardless of the value of Bn and ζ. Nonetheless, the drop in Stokes drag is more significant at a higher Bn when compared to smaller or zero Bn number (see figure 9). Specifically, the relative reduction of $\mathrm{C_s}$ at constant $\zeta = 24$ and $\mathrm{Bn} = 0$, $\mathrm{Bn} = 0.0209$, $\mathrm{Bn} = 0.0417$ from $\mathrm{De} = 1$ to $\mathrm{De} = 0.1$ is 3.63%, 11.41%, and 22.53%. Note also that the relative reduction of the Stokes drag coefficient $\delta\,\mathrm{C_s}$ at $\zeta = 24$, $\mathrm{Bn} = 0$, defined as

$$\delta\,\mathrm{C_s} = \frac{\mathrm{C_s}\left(\zeta = 24, \mathrm{Bn} = 0, \mathrm{De} = 0.1\right) - \mathrm{C_s}\left(\zeta = 24, \mathrm{Bn} = 0, \mathrm{De} = 1\right)}{\mathrm{C_s}\left(\zeta = 24, \mathrm{Bn} = 0, \mathrm{De} = 0.1\right)} \times 100,$$

reveals that even in the absence of wall-effects, the modification of the particle

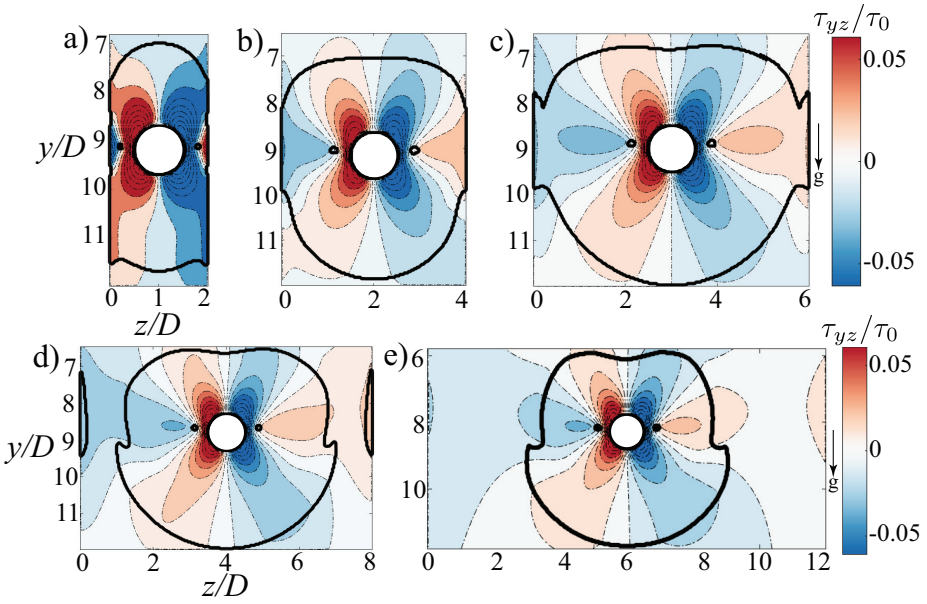

Figure 10: Contour-plots of the shear stress in the mid-$y-z$ plane τ_{yz} normalized by the characteristic stress τ_0 and the unyielded/yielded boundaries (solid black line) at Bn $= 0.0209$, De $= 1$ and at a) $\zeta = 4$, b) $\zeta = 8$, c) $\zeta = 12$, d) $\zeta = 16$, e) $\zeta = 24$.

dynamics at higher levels of elasticity is more pronounced as the plastic effects become more important.

It can be observed from figure figure 9 that the smallest drag is associated with zero Bn number and the largest confinement ratio $\zeta = 24$, where the plastic effect vanishes and the wall-effects are negligible. The value of the Stokes drag coefficient at Bn $= 0$ and $\zeta = 24$ is 1.1238, 1.1012, and 1.0829 for De $= 0.1$, De $= 0.5$, and De $= 1$. Consequently, the EVP material at zero Bn number and $\zeta = 24$ is well approximated as a Newtonian viscous fluid. On the other hand, the value of C_s deviates significantly from 1 (Newtonian fluid) at the highest Bn, lowest De and lowest confinement ratio. Specifically, at $\zeta = 4$, Bn $= 0.0417$, and De $= 0.1$, the Stokes drag coefficient is $C_s = 5.5685$, which is the largest value among all our cases. Thus, the sphere settles at lowest rate for the highest Bn number, smallest confinement ratio ζ, and smallest De number.

In addition, we compare in figure 9 the values of the Stokes drag coefficient C_s

computed here at the largest confinement ratio $\zeta = 24$ and at various degrees of material plasticity and elasticity with the same quantity and at the same values of the Bn and De with the data in [15], which were found by performing transient 2D axisymmetric computations. Note that the numerical values of C_s from [15] are only valid for the largest confinement ratio, *i.e.,* $\zeta = 24$ and for the sphere settling in an EVP material in a tube configuration. Although we find reasonable agreement between our numerical data and the data presented by [15], we speculate that the slight deviation of the Stokes drag coefficient C_s found in our work from the previous study [15] is due to the difference in the flow configuration as we perform 3D numerical simulations in a rectangular box whereas the previous computations were performed in a tube and assuming an axisymmetric flow [15].

We have shown in section 3.1 how the distribution of the fluid velocity around a sphere is affected by the presence of the confining walls. Specifically, the change in both velocity magnitude and the direction of the flow streamlines is more abrupt when the channel walls are brought closer to the particle. This results in a larger shear resistance at a smaller confinement ratio ζ. To further demonstrate this effect, we display in figure 10 the distribution of the shear stress in the central $y-z$ plane, *i.e.,* the τ_{yz} component of the stress tensor, along with the yield surface boundaries around the particle at various ζ and constant Bn and De numbers. By decreasing the wall–particle distance, shear layers develop on the wall of the channel and the magnitude of the shear stress is enhanced around and on the particle surface. The shear layers on the confining walls, as well as the shear stress enhancement on the surface of the sphere, cause the sudden decrease of the particle terminal velocity with decreasing confinement ratio ζ. A similar mechanism has been suggested previously as the primary reason for the sudden decrease of the terminal velocity of a particle settling in a tube filled with an EVP fluid when increasing the Bn number when wall effects are negligible [15].

Based on the results in figures 9, we also note that the sphere settling velocity through an EVP fluid at constant elasticity and confinement ratio ζ and various

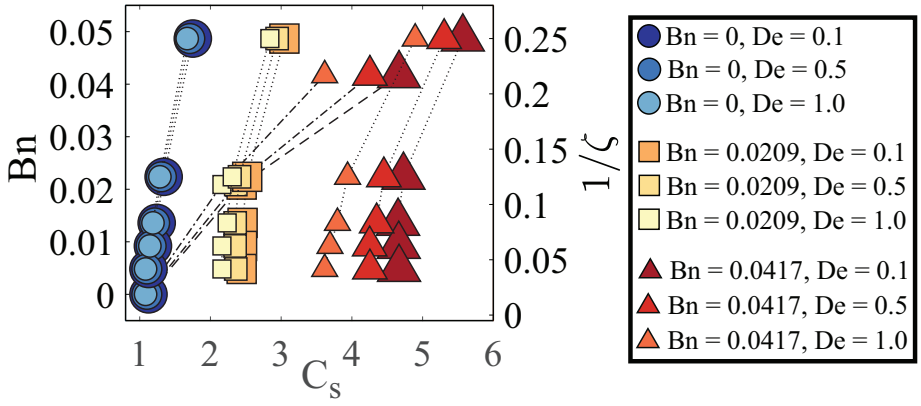

Figure 11: Variation of the Stokes drag coefficient C_s with the Bingham number Bn, inverse of the confinement ratio $1/\zeta$, and the Deborah number De.

Bn numbers is qualitatively the same as if it sediments at constant elasticity and Bn number and various confinement ratio ζ. Indeed, the Stokes drag coefficient increases by either increasing the Bn number at fixed De number and ζ or by decreasing ζ at fixed De and Bn numbers. However, the change in particle dynamics in these two scenarios is quantitatively different. We have shown this difference more clearly in figure 11. The Stokes drag enhancement is more abrupt by increasing Bn and fixing De and the particle-wall distance ($1/\zeta = 0.0417$ in this figure) as compared to increasing $1/\zeta$ and fixing the De, Bn numbers. In figure 11, when the Bn and De numbers are constant, *e.g.,* Bn $= 0$, De $= 0.1$ (dark blue circular markers), the confinement ratio is varying according to the right vertical axis ($1/\zeta$) and the Stokes drag coefficient C_s is shown on the horizontal axis. For a fixed value of the confinement ratio ($1/\zeta = 0.0417$ in this figure) and different De numbers, the Bn number varies according to the left vertical axis (Bn), and the Stokes drag coefficient C_s variation is again shown on the horizontal axis. Contrary to previous suggestions [15], our simulations show that for a single sphere settling in an EVP fluid, the wall and plastic effects on the particle and flow dynamics is quantitatively distinct, and the plasticity has a larger impact than the confinement.

To provide a more quantitative analysis on the effect of confining walls, we

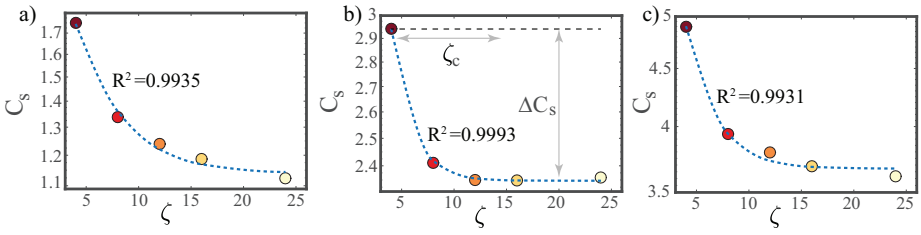

Figure 12: Stokes drag coefficient C_s versus the confinement ratio ζ and the empirical exponential relaxation function (dashed blue line) of the form $C_s = C_s^{max} - \Delta C_s\,(1 - \exp(-\zeta/\zeta_c))$ at a) Bn = 0, De = 0.1, b) Bn = 0.0209, De = 0.5, c) Bn = 0.0417, De = 1.0. The corresponding R^2 values are shown in each panel.

investigate the particle dynamics by fitting an exponential relaxation to the evolution of the Stokes drag coefficient C_s as function of the confinement ratio ζ (see figure 12):

$$C_s\,(\mathrm{Bn}, \mathrm{De}, \zeta) = C_s^{max}\,(\mathrm{Bn}, \mathrm{De}) - \Delta\, C_s\,(\mathrm{Bn}, \mathrm{De})\,(1 - \exp(-\zeta/\zeta_c\,(\mathrm{Bn}, \mathrm{De}))), \tag{11}$$

where C_s^{max} denotes the maximum Stokes drag coefficient at each Bn and De numbers which is the sphere Stokes drag at the smallest confinement ratio, *i.e.,* $\zeta = 4$. $\Delta\, C_s$ corresponds to the maximum variation of C_s by the confinement ratio which is a function of Bn and De. ζ_c is the critical confinement ratio above which the Stokes drag coefficient or equivalently the particle terminal velocity saturates and does not significantly change by further moving the confining walls away from the sphere. In general, this critical value of the particle-wall distance is a function of material plasticity and elasticity. Figure 12 displays examples of the exponential relaxation functions for the Stokes drag coefficients, obtained employing the least square fitting for three values of Bn and De numbers. It can be seen that the exponential decay perfectly follows the simulation data with the R^2 values (a statistical measure that quantifies the accuracy of the fit) around 0.99 for all the cases. Note that a similar trend holds for all of our simulation cases, not shown here for the sake of brevity.

The critical confinement ratios ζ_c and the maximum variations of the Stokes drag coefficient with the confinement ratio, $\Delta\, C_s$, are depicted in the Bn – De

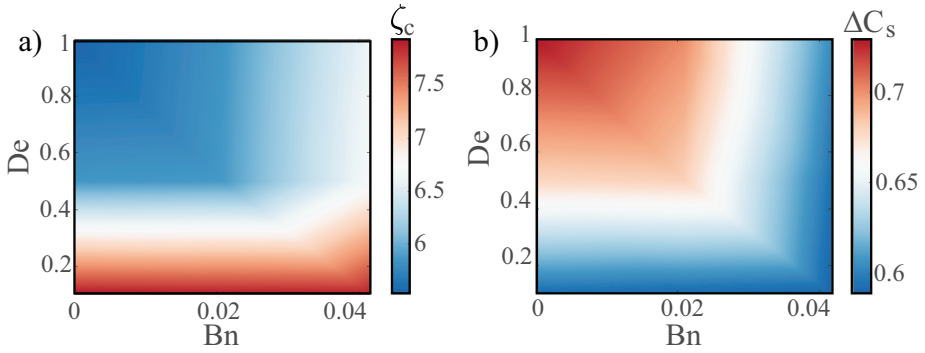

Figure 13: Colormaps of a) the critical confinement ratio ζ_c and b) the maximum change of Stokes drag coefficient, $\Delta\,\mathrm{C_s}$, with the confinement ratio in the Bn – De plane.

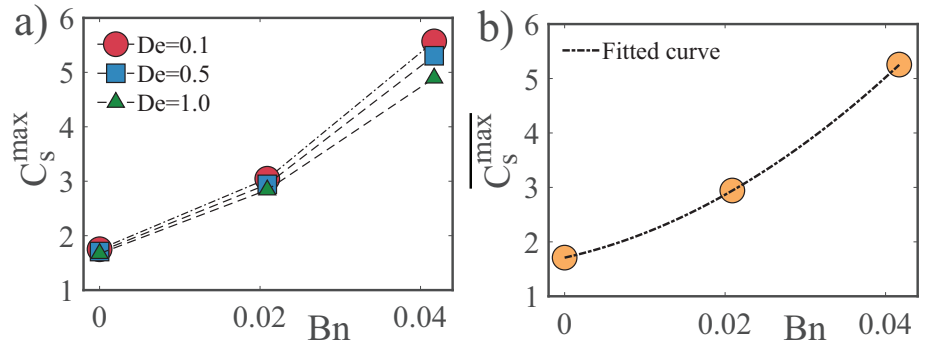

Figure 14: a) Variation of the maximum Stokes drag coefficient $\mathrm{C_s^{max}}$ with the Bn and De numbers. b) Variation of the maximum Stokes drag coefficient averaged over the De number, *i.e.*, $\overline{\mathrm{C_s^{max}}}$, versus the Bingham number Bn with the best fit of the form $\overline{\mathrm{C_s^{max}}}\,(\mathrm{Bn}) = 1.25 \times 10^{-3}\,\mathrm{Bn}^2 + 32.8\,\mathrm{Bn} + 1.71$. The R^2 value for the fitted curve is 0.9995.

plane in figure 13. The data show that although the critical confinement ratio ζ_c and the maximum change of Stokes drag coefficient $\Delta\,\mathrm{C_s}$ are functions of Bn and De numbers, they are weakly dependent of the level of material elasticity and plasticity. The critical confinement averaged over all the Bn and De numbers is $\zeta_c = \overline{\zeta_c} \pm \hat{\sigma}_{\zeta_c} = 6.6944 \pm 1.007$ and the average value of $\Delta\,\mathrm{C_s}$ is $\Delta\,\mathrm{C_s} = \overline{\Delta\,\mathrm{C_s}} \pm \hat{\sigma}_{\Delta\,\mathrm{C_s}} = 0.6406 \pm 0.0564$, where $\hat{\sigma}_{\zeta_c}$ and $\hat{\sigma}_{\Delta\,\mathrm{C_s}}$ denote the standard deviation of ζ_c and $\Delta\,\mathrm{C_s}$. These average values are found by fitting our data points using the least square method.

Because the maximum variation of C_s with the confinement ratio, *i.e.,* ΔC_s and the critical confinement ratio ζ_c are almost constant for the range of Bn and De numbers studied here, equation 11 can be re-written as:

$$C_s\left(Bn, De, \zeta\right) = C_s^{max}\left(Bn, De\right) - \overline{\Delta C_s}\left(1 - \exp\left(-\zeta/\overline{\zeta_c}\right)\right). \tag{12}$$

The variation of the maximum Stokes drag coefficient C_s^{max} by the material placticity and elasticity is displayed in figure 14a. Clearly, C_s^{max} is a strong function of the Bingham number, and a weak function of the Deborah number for the range studied here. In other words, C_s^{max} is almost independent of the material elasticity when $0.1 \leq De \leq 1.0$. In particular, the maximum relative change of C_s^{max} at the highest Bn number ($Bn = 0.0417$) is around 10%. Therefore, we consider the average of C_s^{max} over the De number at each value of Bn. The variation of the average of the maximum Stokes drag coefficient $\overline{C_s^{max}}$ with Bn is depicted in figure 14b with yellow circular markers. Fitting a quadratic function to the simulation data, we obtain $\overline{C_s^{max}}\left(Bn\right) = 1.25 \times 10^{-3}\, Bn^2 + 32.8\, Bn + 1.71$ (see figure 14b). Assuming the maximum Stokes drag coefficient $C_s^{max}\left(Bn, De\right)$ can be well-approximated by $\overline{C_s^{max}}\left(Bn\right)$, the Stokes drag coefficient C_s can be finally written as:

$$C_s\left(Bn, \zeta\right) = \left(1.25 \times 10^{-3}\, Bn^2 + 32.8\, Bn + 1.71\right) - 0.6405\left(1 - \exp\left(-\zeta/6.6938\right)\right). \tag{13}$$

We show in figure 9 that the proposed correlation, *i.e.,* equation (13), fits well with the high-fidelity numerical data points obtained in this study. Note that the above correlation is valid for $0 \leq Bn \leq 0.0417$, $0.1 \leq De \leq 1.0$, and $4 \leq \zeta \leq 24$. Nevertheless, we expect that the average values of the critical confinement and of the maximum change of Stokes drag coefficient remain almost unchanged until the particle stoppage criteria expressed in equation 9 and derived in [15] is satisfied. However, further evidence is required to validate our assumption.

4. Conclusion

High-fidelity numerical simulations are performed to study the role of confinement on the sedimentation of a single sphere through an otherwise quiescent

yield stress fluid with finite elasticity in the limit of negligible inertia. The carrying EVP fluid exhibits elastic, viscous, and plastic behavior simultaneously and are modeled via the Saramito's constitutive equations [1]. We investigate the combined and simultaneous effects of confinement, elasticity, and plasticity on the particle and flow dynamics by performing a total number of 45 interface-resolved simulations. In all of the simulations, the Archimedes number Ar is held low and constant, Ar = 0.5 and find that the maximum value of the particle Reynolds number based on the sphere terminal velocity is $\mathrm{Re}_{\mathrm{U_p}} = 0.2052$, which implies that our simulations are indeed performed at creeping flow condition. Since our main focus is on the wall-effect on the particle and flow dynamics, a wide range of confinement ratios $4 \leq \zeta \leq 24$ is examined. The computational matrix is designed such that the simulations are conducted below the critical condition beyond which the particle is entrapped inside an EVP fluid [15]. Hence the Bingham and Deborah number are set in the range $0 \leq \mathrm{Bn} \leq 0.0417$, and $0.1 \leq \mathrm{De} \leq 1.0$.

As concerns the flow dynamics, the velocity distribution is greatly affected by the presence of the confining walls. In particular, the streamlines are more packed and the size and extent of the recirculation zones in the equatorial plane and on either side of the sphere are significantly altered as the channel walls are brought closer to the sphere surface: the size of the recirculation regions reduces while they interact with and extend to the confining walls as the confinement ratio is decreased. Moreover, the symmetry in the wall-normal direction breaks due to the large wall effects at the lowest level of confinement. We find that the location of the negative wake moves towards the north pole of the sphere as the particle settles in a more confined configuration, which results in a lower particle settling rate.

Similarly to the case of Bingham plastic [13] and Herschel-Bulkley fluids [24], the outer yield envelope extends to the channel walls at small confinement ratios ($\zeta = 4, 8$) for the range of Bn number considered here. Consequently, the fluid velocity relaxes faster at these confinement ratios, and the direction of the streamlines is changed more abruptly as compared to larger confinements. One

of the consequences of the sudden change of velocity magnitude and direction is the sudden increase of the shear stress around the sphere once it sediments in a more confined configuration. In other words, by bringing the channel walls closer to the sphere, the shear resistance increases and shear layers develop on the channel walls and on the yield surface. This phenomenon, *i.e.,* shear layer development on the confining walls when the particle settles through viscoelastic fluid, has been reported before for the case of a particle settling in a tube [29, 30]. Further, we find that the interaction between the yield surface and the confining walls disappears for $\zeta \geq 16$ and $\zeta \geq 12$ at Bn $= 0.0209$ and Bn $= 0.0417$, and thus the confinement effects become weak.

Our computations show that the sphere Stokes drag increases at smaller confinement ratios, with a similar trend at each level of material plasticity and elasticity under investigation here. Also, the largest Stokes drag coefficient occurs at the smallest confinement ratio ζ, largest Bn number, and smallest De number.

Moreover, we find that the settling behavior at fixed Bn number and different confinement ratios follows the same trends as the settling at fixed confinement ratio and various Bn numbers. Although the Stokes drag increases in both cases as mentioned previously in [15], the drag enhancement is more significant for the latter case. One possible explanation for the quantitative difference between these two scenarios is that the yield surface that surrounds the particle acts as an elastic boundary while the confining channel walls are rigid.

By performing a more quantitative analysis on the Stokes drag coefficients, we could fit an exponential relaxation function to the simulation data and identify two parameters: the critical confinement ratio ζ_c and the maximum change of Stokes drag with the confinement ratio $\Delta\, \mathrm{C_s}$ for each Bn and De number. Interestingly, although ζ_c and $\Delta\, \mathrm{C_s}$ are in general functions of Bn and De, they remain approximately constant in the range of the dimensionless numbers investigated here.

We have presented a correlation (equation 13) for the Stokes drag coefficient $\mathrm{C_s}$ of a single spherical particle settling in a laboratory yield-stress fluid as

a function of material plasticity (Bn number), and confinement ratio ζ; this is obtained with a non-linear regression of our simulation data. This expression can be considered as the main achievement of this study. The proposed correlation is valid for $0 \leq \mathrm{Bn} \leq 0.0417$, $0.1 \leq \mathrm{De} \leq 1.0$, and $4 \leq \zeta \leq 24$ and $\mathrm{Ar} = 0.5$. Although the Stokes drag $\mathrm{C_s}$ is also a function of the material elasticity (see figure 9), we find that this dependency is weak and thus can be neglected for $0.1 \leq \mathrm{De} \leq 1.0$. Therefore, the suggested correlation is independent of De number.

We hope this study may open an avenue to answer many fundamental questions on the particle dynamics in practical yield stress fluids, *e. g.,* concerning the effect of confining walls, elasticity, and plasticity on the sphere drag, the drag laws when interactions between particles and walls are present, and particle migration when inertia becomes more important. Moreover, this study provides useful quantitative information about the minimum requirements of the dimensions of an experimental apparatus (rectangular box in this case) to address the particle dynamics in laboratory yield-stress fluids such that confinement effects can be neglected. Furthermore, we present the vertical distance travelled in the settling direction and the time required to reach the steady state for various combinations of dimensionless numbers, which can further help to design the experimental apparatus. We present estimates for the sphere drag before the particle entrapment occurs which can be helpful to test the validity of existing EVP models and to modify the particle stoppage criteria when confinement is important. Finally, particle-particle and particle-wall interactions in a dense suspension rather than a dilute one are also interest topics for future studies.

Acknowledgements

M. E. R. was supported by the Okinawa Institute of Science and Technology Graduate University (OIST) with subsidy funding from the Cabinet Office, Government of Japan. L.B. acknowledges the support from the by the Swedish Research Council, via the multidisciplinary research environment INTERFACE

(VR 2016-06119, Hybrid multiscale modelling of transport phenomena for energy efficient processes).

Declaration of interests

The authors report no conflict of interest.

References

[1] P. Saramito, A new elastoviscoplastic model based on the herschel–bulkley viscoplastic model, Journal of Non-Newtonian Fluid Mechanics 158 (1-3) (2009) 154–161.

[2] D. Bonn, M. M. Denn, Yield stress fluids slowly yield to analysis, Science 324 (5933) (2009) 1401–1402.

[3] P. Coussot, J. Raynaud, F. Bertrand, P. Moucheront, J. Guilbaud, H. Huynh, S. Jarny, D. Lesueur, Coexistence of liquid and solid phases in flowing soft-glassy materials, Physical review letters 88 (21) (2002) 218301.

[4] B. Gueslin, L. Talini, B. Herzhaft, Y. Peysson, C. Allain, Flow induced by a sphere settling in an aging yield-stress fluid, Physics of Fluids 18 (10) (2006) 103101.

[5] B. Dollet, F. Graner, Two-dimensional flow of foam around a circular obstacle: local measurements of elasticity, plasticity and flow, Journal of Fluid Mechanics 585 (2007) 181–211.

[6] A. Putz, T. Burghelea, I. Frigaard, D. Martinez, Settling of an isolated spherical particle in a yield stress shear thinning fluid, Physics of Fluids 20 (3) (2008) 033102.

[7] D. Sikorski, H. Tabuteau, J. R. de Bruyn, Motion and shape of bubbles rising through a yield-stress fluid, Journal of Non-Newtonian Fluid Mechanics 159 (1-3) (2009) 10–16.

[8] G. Benmouffok-Benbelkacem, F. Caton, C. Baravian, S. Skali-Lami, Non-linear viscoelasticity and temporal behavior of typical yield stress fluids: Carbopol, xanthan and ketchup, Rheologica acta 49 (3) (2010) 305–314.

[9] Y. Holenberg, O. M. Lavrenteva, U. Shavit, A. Nir, Particle tracking velocimetry and particle image velocimetry study of the slow motion of rough and smooth solid spheres in a yield-stress fluid, Physical Review E 86 (6) (2012) 066301.

[10] P. Saramito, A new constitutive equation for elastoviscoplastic fluid flows, Journal of Non-Newtonian Fluid Mechanics 145 (1) (2007) 1–14.

[11] I. Cheddadi, P. Saramito, F. Graner, Steady couette flows of elastoviscoplastic fluids are nonunique, Journal of rheology 56 (1) (2012) 213–239.

[12] A. Beris, J. Tsamopoulos, R. Armstrong, R. Brown, Creeping motion of a sphere through a bingham plastic, Journal of Fluid Mechanics 158 (1985) 219–244.

[13] J. Blackery, E. Mitsoulis, Creeping motion of a sphere in tubes filled with a bingham plastic material, Journal of non-newtonian fluid mechanics 70 (1-2) (1997) 59–77.

[14] B. T. Liu, S. J. Muller, M. M. Denn, Convergence of a regularization method for creeping flow of a bingham material about a rigid sphere, Journal of non-newtonian fluid mechanics 102 (2) (2002) 179–191.

[15] D. Fraggedakis, Y. Dimakopoulos, J. Tsamopoulos, Yielding the yield-stress analysis: a study focused on the effects of elasticity on the settling of a single spherical particle in simple yield-stress fluids, Soft matter 12 (24) (2016) 5378–5401.

[16] M. Sarabian, M. E. Rosti, L. Brandt, S. Hormozi, Numerical simulations of a sphere settling in simple shear flows of yield stress fluids, Journal of Fluid Mechanics 896.

[17] H. Faxén, Der widerstand gegen die bewegung einer starren kugel in einer zähen flüssigkeit, die zwischen zwei parallelen ebenen wänden eingeschlossen ist, Annalen der Physik 373 (10) (1922) 89–119.

[18] A. Miyamura, S. Iwasaki, T. Ishii, Experimental wall correction factors of single solid spheres in triangular and square cylinders, and parallel plates, International Journal of Multiphase Flow 7 (1) (1981) 41–46.

[19] C. W. Oseen, Neuere methoden und ergebnisse in der hydrodynamik, Leipzig: Akademische Verlagsgesellschaft mb H.

[20] K. Yeo, M. R. Maxey, Anomalous diffusion of wall-bounded non-colloidal suspensions in a steady shear flow, EPL (Europhysics Letters) 92 (2) (2010) 24008.

[21] M. Sarabian, M. Firouznia, B. Metzger, S. Hormozi, Fully developed and transient concentration profiles of particulate suspensions sheared in a cylindrical couette cell, Journal of Fluid Mechanics 862 (2019) 659–671.

[22] M. Sarabian, Experimental Investigations and Direct Numerical Simulations of Rigid Particles in Shear Flows of Newtonian and Complex Fluids, Ohio University, 2020.

[23] A. Rashedi, M. Sarabian, M. Firouznia, D. Roberts, G. Ovarlez, S. Hormozi, Shear-induced migration and axial development of particles in channel flows of non-brownian suspensions, AIChE Journal 66 (12) (2020) e17100.

[24] M. Beaulne, E. Mitsoulis, Creeping motion of a sphere in tubes filled with herschel–bulkley fluids, Journal of non-newtonian fluid mechanics 72 (1) (1997) 55–71.

[25] D. Atapattu, R. Chhabra, P. Uhlherr, Creeping sphere motion in herschel-bulkley fluids: flow field and drag, Journal of non-newtonian fluid mechanics 59 (2-3) (1995) 245–265.

[26] A. Wachs, I. A. Frigaard, Particle settling in yield stress fluids: limiting time, distance and applications, Journal of Non-Newtonian Fluid Mechanics 238 (2016) 189–204.

[27] H. Tabuteau, P. Coussot, J. R. de Bruyn, Drag force on a sphere in steady motion through a yield-stress fluid, Journal of rheology 51 (1) (2007) 125–137.

[28] F. Ahonguio, L. Jossic, A. Magnin, Influence of surface properties on the flow of a yield stress fluid around spheres, Journal of Non-Newtonian Fluid Mechanics 206 (2014) 57–70.

[29] W. Lunsmann, L. Genieser, R. Armstrong, R. Brown, Finite element analysis of steady viscoelastic flow around a sphere in a tube: calculations with constant viscosity models, Journal of non-newtonian fluid mechanics 48 (1-2) (1993) 63–99.

[30] O. G. Harlen, The negative wake behind a sphere sedimenting through a viscoelastic fluid, Journal of Non-Newtonian Fluid Mechanics 108 (1-3) (2002) 411–430.

[31] P. Huang, J. Feng, Wall effects on the flow of viscoelastic fluids around a circular cylinder, Journal of non-newtonian fluid mechanics 60 (2-3) (1995) 179–198.

[32] G. H. McKinley, Steady and transient motion of spherical particles in viscoelastic liquids, Transport Processes in Bubble, Drops, and Particles (2002) 338–375.

[33] A. W. Liu, Viscoelastic flow of polymer solutions around arrays of cylinders: comparison of experiment and theory, Ph. D. Thesis (1997) 6095.

[34] J.-M. Piau, Carbopol gels: Elastoviscoplastic and slippery glasses made of individual swollen sponges: Meso-and macroscopic properties, constitutive equations and scaling laws, Journal of non-newtonian fluid mechanics 144 (1) (2007) 1–29.

[35] S. Chen, N. Phan-Thien, B. C. Khoo, X. J. Fan, Flow around spheres by dissipative particle dynamics, Physics of Fluids 18 (10) (2006) 103605.

[36] W.-P. Breugem, A second-order accurate immersed boundary method for fully resolved simulations of particle-laden flows, Journal of Computational Physics 231 (13) (2012) 4469–4498.

[37] T. Zisis, E. Mitsoulis, Viscoplastic flow around a cylinder kept between parallel plates, Journal of non-newtonian fluid mechanics 105 (1) (2002) 1–20.

[38] E. Mitsoulis, On creeping drag flow of a viscoplastic fluid past a circular cylinder: wall effects, Chemical engineering science 59 (4) (2004) 789–800.

[39] D. Izbassarov, M. E. Rosti, M. N. Ardekani, M. Sarabian, S. Hormozi, L. Brandt, O. Tammisola, Computational modeling of multiphase viscoelastic and elastoviscoplastic flows, International Journal for Numerical Methods in Fluids 88 (12) (2018) 521–543.

[40] J. Kim, P. Moin, Application of a fractional-step method to incompressible navier-stokes equations, Journal of computational physics 59 (2) (1985) 308–323.

[41] C.-W. Shu, High order weighted essentially nonoscillatory schemes for convection dominated problems, SIAM review 51 (1) (2009) 82–126.

[42] M. E. Rosti, L. Brandt, Numerical simulation of turbulent channel flow over a viscous hyper-elastic wall, Journal of Fluid Mechanics 830 (2017) 708–735.

[43] I. Lashgari, F. Picano, W.-P. Breugem, L. Brandt, Laminar, turbulent, and inertial shear-thickening regimes in channel flow of neutrally buoyant particle suspensions, Physical review letters 113 (25) (2014) 254502.

[44] M. E. Rosti, P. Mirbod, L. Brandt, The impact of porous walls on the rheology of suspensions, Chemical Engineering Science 230 (2020) 116178.

[45] M. E. Rosti, L. Brandt, Increase of turbulent drag by polymers in particle suspensions, Physical Review Fluids 5 (4) (2020) 041301.

[46] D. Alghalibi, I. Lashgari, L. Brandt, S. Hormozi, Interface-resolved simulations of particle suspensions in newtonian, shear thinning and shear thickening carrier fluids, Journal of Fluid Mechanics 852 (2018) 329–357.

[47] M. E. Rosti, D. Izbassarov, O. Tammisola, S. Hormozi, L. Brandt, Turbulent channel flow of an elastoviscoplastic fluid, Journal of Fluid Mechanics 853 (2018) 488–514.

[48] A. Shahmardi, S. Zade, M. N. Ardekani, R. J. Poole, F. Lundell, M. E. Rosti, L. Brandt, Turbulent duct flow with polymers, Journal of Fluid Mechanics 859 (2019) 1057–1083.

[49] F. De Vita, M. E. Rosti, D. Izbassarov, L. Duffo, O. Tammisola, S. Hormozi, L. Brandt, Elastoviscoplastic flows in porous media, Journal of Non-Newtonian Fluid Mechanics 258 (2018) 10–21.

[50] S. Padhy, E. Shaqfeh, G. Iaccarino, J. Morris, N. Tonmukayakul, Simulations of a sphere sedimenting in a viscoelastic fluid with cross shear flow, Journal of Non-Newtonian Fluid Mechanics 197 (2013) 48–60.

[51] R. W. Ansley, T. N. Smith, Motion of spherical particles in a bingham plastic, AIChE Journal 13 (6) (1967) 1193–1196.